

# Einstein–de Haas torque as a discrete spectroscopic probe allows nanomechanical measurement of a magnetic resonance

K. R. Fast<sup>1,2</sup>, J. E. Losby<sup>2,3</sup>, G. Hajisalem<sup>2,3</sup>, P. E. Barclay<sup>2,3,\*</sup> and M. R. Freeman<sup>1,2,†</sup>

<sup>1</sup>*Department of Physics, University of Alberta, Edmonton, Alberta T6G 2E1, Canada*

<sup>2</sup>*Nanotechnology Research Centre, National Research Council of Canada, Edmonton, Alberta T6G 2M9, Canada*

<sup>3</sup>*Department of Physics and Astronomy, University of Calgary, Calgary, Alberta T2N 1N4, Canada*



(Received 27 October 2023; revised 15 January 2024; accepted 18 January 2024; published 5 February 2024)

The Einstein–de Haas (EdH) effect is a fundamental, mechanical consequence of any temporal change of magnetism in an object. EdH torque results from conserving the object's total angular momentum: The angular momenta of all the specimen's magnetic moments, together with its mechanical angular momentum. Although the EdH effect is usually small and difficult to observe, it increases in magnitude with detection frequency. We explore the frequency dependence of EdH torque for a thin film permalloy microstructure by employing a ladder of flexural beam modes (with five distinct resonance frequencies spanning from 3 to 208 MHz) within a nanocavity optomechanical torque sensor via magnetic hysteresis curves measured at mechanical resonances. At low dc fields, the gyrotropic resonance of a magnetic vortex spin texture overlaps the 208 MHz mechanical mode. The massive EdH mechanical torques arising from this coresonance yield a fingerprint of vortex core pinning and depinning in the sample. The experimental results are discussed in relation to mechanical torques predicted from both macrospin (at high dc magnetic field) and finite-difference solutions to the Landau-Lifshitz-Gilbert (LLG) equation. A global fit of the LLG solutions to the frequency-dependent data reveals a statistically significant discrepancy between the experimentally observed and simulated torque phase behaviours at spin-texture transitions that can be reduced through the addition of a time constant to the conversion between magnetic cross-product torque and mechanical torque, constrained by experiment to be in the range of 0.5–4 ns.

DOI: [10.1103/PhysRevB.109.064404](https://doi.org/10.1103/PhysRevB.109.064404)

## I. INTRODUCTION

The Einstein–de Haas (EdH) effect is the result of a landmark gyromagnetic investigation conducted just over a century ago that established the fundamental connection between magnetism and mechanical angular momentum [1]. In the EdH experiment, mechanical rotation of a suspended ferromagnetic body was observed as it underwent an alternating change in net magnetization at the torsional resonance frequency. The effect was very small and, in the first observation, subject to systematic experimental uncertainty comparable in magnitude to the measured torque. Regrowing interest in the EdH effect [2–10] has emerged with the miniaturization of torque sensors through micro- and nanofabrication [4,11–16]. Small mechanical sensors couple well to magnetic torques generated in small magnetic specimens affixed to them [17]. Micromechanical EdH investigations by Wallis *et al.* determined the magnetomechanical ratio (the inverse of the gyromagnetic ratio) of a thin film of permalloy deposited on a silicon nitride cantilever [2]. In another investigation, spin-wave currents induced through the spin-Seebeck effect transferred angular momentum to a mechanical resonator created in bulk yttrium iron garnet [18]. In these cases, the mechanical resonance frequencies of the sensors were on

the order of tens of kilohertz. Advances in nanomechanical sensing and, particularly, the incorporation of cavity optomechanical readouts [19–23], have introduced the displacement sensitivity needed for mechanical probes of physical phenomena to progress to radio and microwave frequencies, overcoming the challenge from amplitudes of driven motion generally decreasing as oscillation frequencies increase.

Measurements to higher driving frequencies expand the scope of what can be learned about magnetism through mechanical sensing of torque. EdH torques grow with frequency and probe ac magnetic susceptibilities via the intrinsic angular momentum embedded and locked to the magnetization. At high-enough frequencies, spin resonances should be observable directly through mechanical torque, and information may emerge about the conversion from magnetic to mechanical drive torque.

Mechanically sensed, ac magnetic field-driven cross-product torque is a probe of magnetic anisotropy. The ac cross-product torques are frequency independent when the system remains close to magnetic equilibrium—that is, without thermally activated, slow dynamics and far enough from spin resonances. The ac EdH torques, in contrast, increase linearly with frequency in the same regime. Nanomechanical EdH measurements at 2.7 MHz demonstrated that the effect can be comparable to or even larger in magnitude than conventional cross-product magnetic torques in nearly demagnetized yttrium iron garnet microdisks at low dc applied fields, and confirmed the 90° phase difference expected between these

\*pbarclay@ucalgary.ca

†freemanm@ualberta.ca

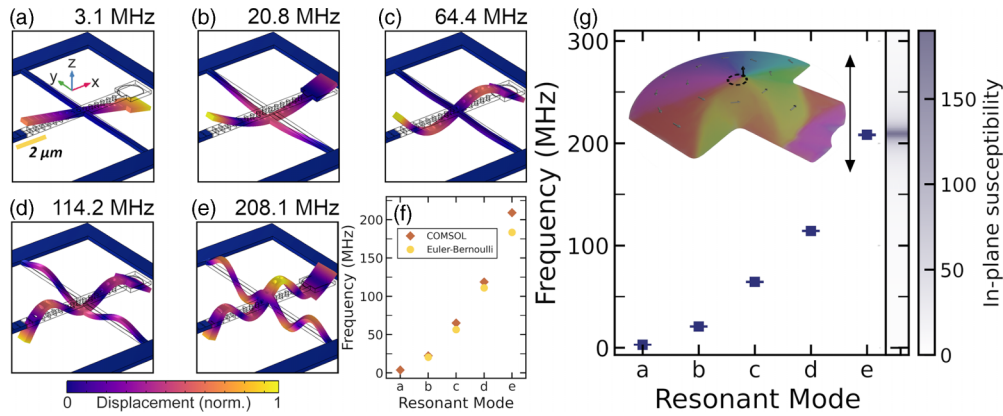


FIG. 1. Mechanical displacement profiles of the multimodal RF mechanical torque sensor. (a) The fundamental torsional mode. A thin-film island of permalloy ( $\text{Ni}_{80}\text{Fe}_{20}$ ) is deposited on the paddle of the free end (outlined on the right side of the stationary resonator wire-frame view). [(b)–(e)] Higher order free-free beam mode profiles. (f) Mode frequencies of [(a)–(e)] computed by finite-element analysis in COMSOL MULTIPHYSICS [29] (filled diamonds) and predicted by Euler-Bernoulli theory assuming free-free boundary conditions (filled circles). (g) Mode frequencies from experiment; error bars indicate resonance linewidth. Simulation of dimensionless magnetic susceptibility over the experimental frequency range at a dc bias field of 2.39 kA/m is indicated by the color bar on the right axis. A magnetic resonance (as illustrated by the cartoon in the upper panel where an RF-field driven magnetic vortex orbits around its equilibrium position) overlaps the 208 MHz mechanical mode. Simulated magnetic resonance frequencies for bias fields between 0 and 15 kA/m are indicated by the black arrow.

two sources of torque when their respective driving fields are in phase [8]. Even for magnetically saturated specimens, the EdH component in an ac torque study is expected to grow from negligible at kHz frequencies into the dominant source of torque when a spin resonance overlaps the mechanical detection frequency and where the resonant enhancement of ac magnetization enables the direct mechanical detection of nonequilibrium magnetism. Torque magnetometry performed at such frequencies could enable coherent coupling of mechanics and spin, as well as open potential pathways for mechanical control of magnetism [24,25].

### A. Multimodal torque sensor

Continuously swept frequency measurements would require torque sensitivity away from mechanical resonances at a level that has not yet been demonstrated. Alternatively, observations at the discrete frequencies within a ladder of resonance modes could permit coresonant detection of mechanical and spin resonances through higher order mechanical modes, as well as utilizing the benefit of EdH torque scaling with frequency. The nanocavity optomechanical torque sensor used in Refs. [26,27] is suited to such a study. Our torque sensor geometry and the spatial displacement profiles of the mechanical mode ladder used for torque measurements are shown in Fig. 1. At the heart of the sensor is a nanomechanical silicon beam along the  $x$  direction, with a paddle at one end to host the magnetic specimen—here, a mushroom-shaped thin-film permalloy ( $\text{Ni}_{80}\text{Fe}_{20}$ ) island. The sensor beam is suspended from its middle by a symmetrical pair of silicon torsion bars along the  $y$  direction. This central mounting of the beam is key to observing a series of mechanical modes at different frequencies, all driven by radio frequency (RF) magnetic  $y$  torques from the sample. The other crucial feature is the optical nanocavity at the other end of the sensor beam, to detect the ensuing

mechanical oscillations. 1D photonic crystal mirrors are embedded in a split-beam geometry and create an optical cavity with maximum field magnitude in the gap between the sensor and stationary beams [28]. The lowest-frequency mechanical resonance mode is the fundamental torsional mode shown in Fig. 1(a). The mode ladder beyond the fundamental torsion resonance exploits the similarity of the suspended sensor's mechanical modes to those of a beam with free ends, thanks to cooperative flexing of the side supports. These modes are all responsive to  $y$ -directed RF torque, arising both from the cross products between  $H_z^{\text{RF}}$  fields and  $x$ -directed net magnetic moment, as well as from  $H_y^{\text{RF}}$ -driven EdH torques. The optical nanocavity has sufficient displacement sensitivity to detect the first four modes in the ladder, at 21, 64, 114, and 208 MHz; the corresponding eigenmodes found by finite-element simulation with COMSOL MULTIPHYSICS [29] are shown in Figs. 1(b)–1(e). Mode frequencies predicted by the Euler-Bernoulli approximation for a thin beam calculated using the material and structural parameters of the sensor (see Supplemental Material [30]) are also displayed in Fig. 1(f) alongside the experimentally measured (Supplemental Material [30]) and COMSOL-estimated eigenmode frequencies. The Euler-Bernoulli formula yields rough agreement with measured mode frequencies, with higher discrepancies when the support beam undergoes more twisting and there is a node in the sensor beam displacement profile at the intersection point [Figs. 1(c) and 1(e)] that is unaccounted for in the Euler-Bernoulli boundary conditions.

### B. Basic expectations for frequency and field dependencies of EdH and cross product torques

Contemporary studies of EdH mechanical torques have been restricted to fully or partially demagnetized specimens, which are driven around minor hysteresis loops by an RF field to yield an oscillating magnitude of net magnetic moment.

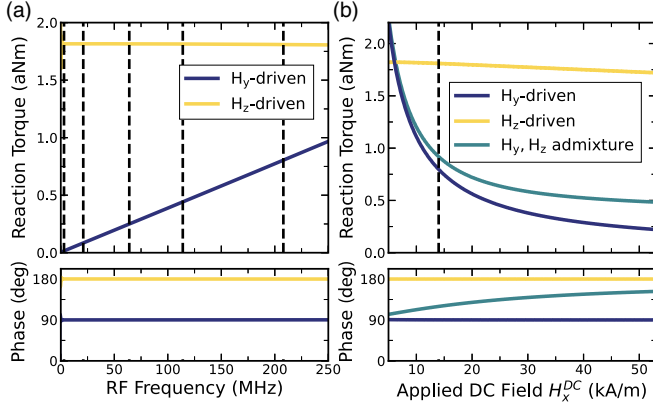


FIG. 2. Macrospin simulation results. Frequency (a) and dc field (b) dependencies of simulated macrospin reaction torques for a 470 nm diameter permalloy sphere with uniaxial hard axis anisotropy along  $\hat{z}$ , uniaxial anisotropy constant  $K_u = 340$  kJ/m<sup>3</sup>, saturation magnetization  $M_s = 767$  kA/m, and Gilbert damping  $\alpha = 0.01$ . The dashed lines in (a) indicate experimentally measured frequencies of the torque sensor used in this paper (3.1, 20.8, 64.4, 114.2, and 208.1 MHz). The dc field of 14 kA/m used in (a) is indicated by a dashed line in (b). The dc field sweeps in (b) are calculated for a drive frequency of 208 MHz. Admixture of  $H_y$ - and  $H_z$ -driven torques are shown in teal for a  $H_y^{\text{RF}}$  amplitude of 50 A/m and a  $H_z^{\text{RF}}$  amplitude of 12.5 A/m. The resultant phase of the admixture-driven torque has a significant dependence on the applied dc field, in contrast to the constant phases of the purely  $H_y$ - and  $H_z$ -driven torques.

In addition, the drive frequencies have been low enough to assume that the magnetization remains in [2,8,31] or close to [8] (i.e., slow dynamics assisted by thermal activation) equilibrium with the applied dc and RF magnetic fields. To gain insight into the conventional and EdH torque contributions under arbitrary drive conditions, we developed and applied a macrospin model to solve the Landau-Lifshitz-Gilbert (LLG) equation for torques in the limit where an almost uniformly magnetized specimen can be approximated by a single, giant spin subject to the sample's magnetic anisotropies (see Supplemental Material [30]). The macrospin code executes hundreds of times faster than a corresponding finite-difference micromagnetic LLG simulation. Solutions for RF drives are passed through a software lock-in emulator to extract torque magnitudes and phases (the same format as the experimental data; details in the Supplemental Material [30]).

Mechanical reaction torques consist of the external field contributions from the full solutions to the LLG equation plus the EdH, angular momentum-conserving contributions. For a simulation set up to mimic our experiment, we focus on the torque component in the plane of the thin film and perpendicular to the  $x$ -directed dc field ( $\hat{y}$ ). This component ( $y$  torque in our coordinate system) drives all five of the mechanical modes used in the measurements reported here. The resultant  $y$  torques are computed for two directions of ac field drive: along  $\hat{z}$  in the traditional cross product  $y$ -torque configuration and along  $\hat{y}$  in the EdH configuration.

Predicted resultant torque magnitudes and phases for two different cuts through experimental parameter space are shown in Fig. 2 for a spherical macrospin having the same

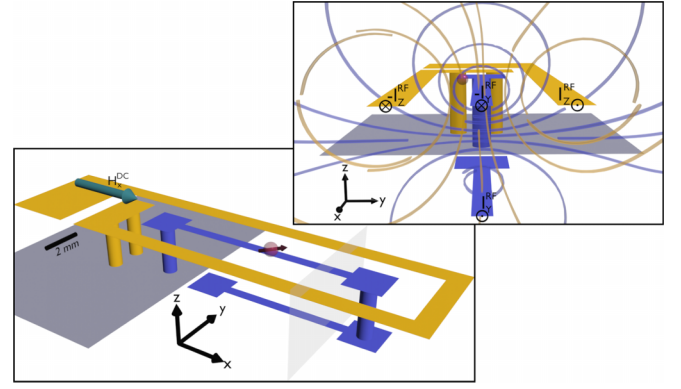


FIG. 3. Strip line field coil geometry. The design of the transmission lines providing RF fields to the sample is shown. Two separate coil loops are present on a single circuit board. Input and return currents are indicated in the upper figure as  $\pm I_z^{\text{RF}}$  (yellow coil) and  $\pm I_y^{\text{RF}}$  (purple coil). The ground plane is shown in gray. Magnetic field lines from each coil (calculated with COMSOL MULTIPHYSICS [29]) are shown in the top panel and illustrate the admixtures of  $z$ - and  $y$ -drive field components at the sample location (indicated by the red sphere).

total moment as the permalloy island and with a uniaxial hard axis along  $\hat{z}$ . The anisotropy energy density equivalent to the shape anisotropy of the microstructure, which has demagnetizing factors  $N_x = 0.042$ ,  $N_y = 0.045$ , and  $N_z = 0.913$ , is  $-340$  kJ/m<sup>3</sup>. A 50 A/m ac field is applied along  $\hat{z}$  ( $H_z$ ) or  $\hat{y}$  ( $H_y$ ) to promote conventional or EdH torques about the  $\hat{y}$  axis. As seen in Fig. 2(a), at frequencies in the range of 100 MHz the EdH torque generated by  $H_y$  is not a small effect, it is in the same order of magnitude as the cross product torque. This is noteworthy because for these parameters, where the dc applied field is small compared to the effective field from the uniaxial anisotropy, the resultant torque generated by  $H_z$  is very close to the maximum value possible for that amplitude of drive. The  $H_y$ -driven torque is also phase shifted by 90° relative to the drive phase.

As a function of increasing dc field strength [Fig. 2(b)], the  $H_z$ -driven cross product torque decreases slowly as the angular excursion of the moment is reduced by the dc field below the limit set at zero field by the magnetic anisotropy. The  $H_y$ -driven EdH torque decreases more rapidly with dc field because the angular excursion of the moment in the easy plane is set by  $H_x$ . An admixture of  $H_y$ - and  $H_z$ -driven torques similar to experimental conditions produces torques which exhibit qualitative similarity (in both magnitude and phase) to measured torques in the quasisaturated spin texture [Fig. 4(c)].

## II. MAGNETIC TORQUE OBSERVATIONS

A dc bias field in the  $x$  direction is provided by a permanent magnet mounted on a linear translation stage. Hysteresis measurements are acquired by sweeping the permanent magnet. The thin film permalloy micromagnet self-demagnetizes in low field and therefore is sufficient to measure unipolar hysteresis loops.

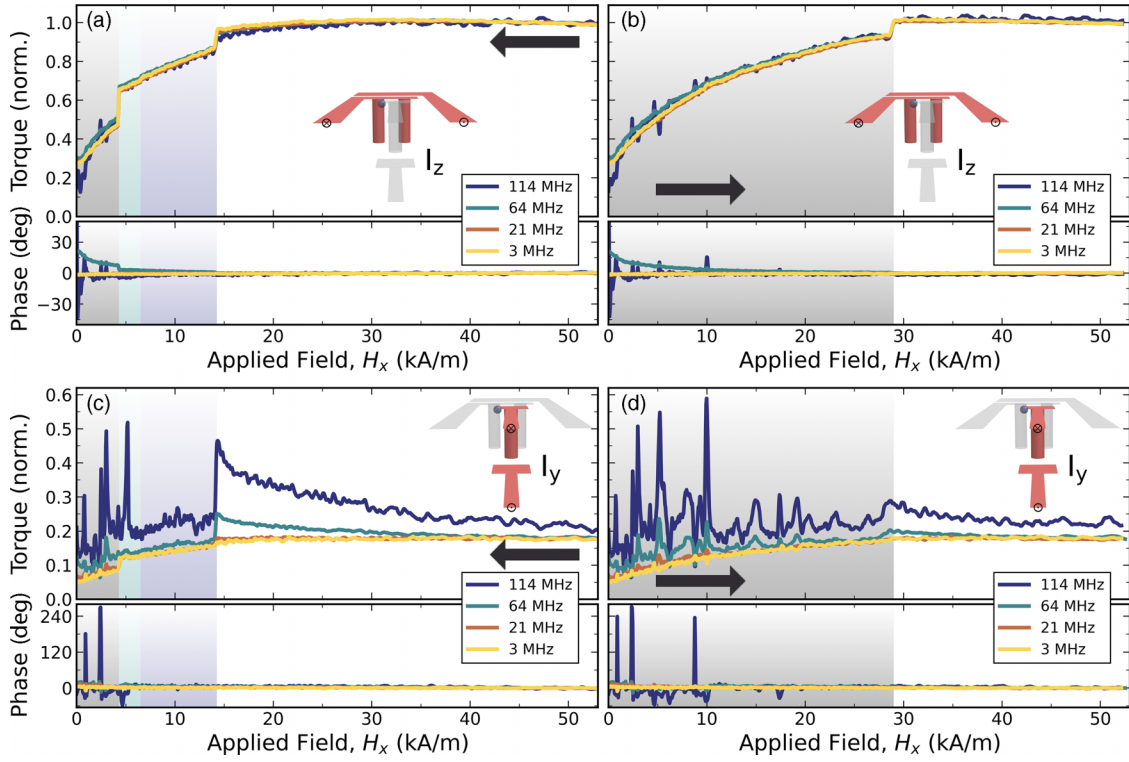


FIG. 4. Torque measurements of hysteresis at 3, 21, 64, and 114 MHz for two orientations of RF drive field. High to low field (a), (c) and reverse direction (b), (d) hysteresis for the  $I_z^{\text{RF}}$ - (a), (b) and  $I_y^{\text{RF}}$ - (c), (d) driven modes up to 114 MHz, with corresponding phase signals in the lower panel of each quadrant. Spin textures present throughout the field sweeps are highlighted with different background shading. The unshaded section is the quasiuniform magnetization texture, the purple is the nucleation of vortex core topologies near the edge of the disk, the blue is the single-vortex nucleation and transition region, and the gray is a single-vortex after relaxation of magnetization in another part of the sample. The drive coil used in each case is highlighted in red in the corresponding inset schematic.

For transduction, a dimple created at the center of a tapered section of optical fiber is placed on the stationary beam mirror to couple light into the photonic crystal cavity. The fiber-coupled laser wavelength is tuned to a position of maximum slope at the cavity resonance in the fiber's transmission spectrum, such that the perturbations of the optical field from beam vibrations are encoded in the intensity and can be read out using lock-in detection [26,27]. We apply magnetic torques to the permalloy island using a custom built, multilayer circuit board (Fig. 3) with single-turn transmission line coils for generating RF magnetic fields in the  $\hat{y}$  and  $\hat{z}$  directions. Respectively, an RF current  $I_y^{\text{RF}}$  ( $I_z^{\text{RF}}$ ) applied to the vertical coil (horizontal coil) yields a predominantly  $H_y^{\text{RF}}$  ( $H_z^{\text{RF}}$ ) magnetic drive field at the sample location, with a small admixture of  $H_z^{\text{RF}}$  ( $H_y^{\text{RF}}$ ). The present experimental setup does *not* have a means for determining the absolute drive field phases at the sample position. We confirmed through sniffer coil measurements with lock-in detection that the  $H_z^{\text{RF}}$  and  $H_y^{\text{RF}}$  drive fields are accurately in phase with one another at the sample, and the experiment therefore has good sensitivity to changes in the relative phases of the EdH and cross product torques (Supplemental Material [30]).

Some parasitic coupling between the RF drives and the photoreceiver exists in the setup and is characterized by companion measurements acquired with the laser tuned away from the optical cavity resonance, to minimize the mechanical

signal. The mechanically-transduced signal magnitudes and phases are then obtained by phasor subtracting the tuned-away backgrounds from the signals at optimal optomechanical coupling (see Supplemental Material [30]).

#### A. Measurements at 3, 21, 64, and 114 MHz modes: Frequency dependence of EdH torque

Normalized hysteresis loops initialized at high field for the 3, 21, 64, and 114 MHz mechanical modes are shown in Fig. 4. The normalization method takes advantage of the drive field admixtures and is described in detail in Supplemental Material [30]. Complementary information from micromagnetic simulations of hysteresis (discussed in the Supplemental Material [30]) is indicated by background shadings corresponding to distinct spin textures. With decreasing field [Figs. 4(a) and 4(c)], the spin-texture transitions from a quasi-single-domain state (unshaded region) into the nucleation of magnetic vortex corelike topologies in the spin texture near the sample edge, around 14 kA/m (purple-shaded region). Further decreasing the field pushes the cores continuously away from the edge until a sharp transition near 6.5 kA/m yields another sizable jump in demagnetization and a single vortex state in the cap of the permalloy mushroom and a quasiuniform state in the stem akin to a thick domain wall (blue-shaded region). An additional transition occurs near 4 kA/m, where the vortex core jumps close to the center of the film, leaving a narrower

domain wall in the stem (gray-shaded region). A final transition into a texture supporting three domains in the stem while maintaining a vortex configuration in the cap occurs infrequently during the data collection at very low bias field and can be identified from its distinct signature (details in the Supplemental Material [30]). When the field sweep direction is reversed at low bias field [Figs. 4(b) and 4(d)], the vortex core trajectory reverses and it translates back towards the edge of the sample until it is annihilated (gray-shaded to unshaded field region).

The frequency dependence of the hysteresis loop shapes is notably different between the  $I_z^{\text{RF}}$ - and  $I_y^{\text{RF}}$ -driven torques. First, we concentrate on the unshaded, higher bias field regions in Fig. 4. On account of the strong easy plane shape anisotropy of the permalloy island, the  $I_z^{\text{RF}}$ -driven signal [seen in Figs. 4(a) and 4(b)] arises predominantly from conventional cross-product torques; it is nearly frequency independent and approximately proportional to the net magnetization along the  $x$  direction (as discussed in the Supplemental Material [30]). The unipolar hysteresis shape is commonly observed for cases of vortex nucleation and annihilation in confined micromagnets [32].

The  $I_y^{\text{RF}}$ -driven hysteresis, on the other hand, has a significant frequency dependence arising from EdH torques. Whereas the 3 MHz curve strongly resembles all  $I_z^{\text{RF}}$ -driven curves (Supplemental Material [30]), higher frequency curves exhibit additional behaviors. The quasiuniform magnetization regime persists over the widest field range in the hysteresis branch sweeping from high field to low field [Figs. 4(a) and 4(c)], until nucleation of a vortex corelike object. In the higher field region, we observe a new contribution to the torque magnitude varying inversely with bias field and increasing with frequency—two of the features found in the macrospin simulations. A surprise in these data is the near constancy (bias field independence) of the  $I_y^{\text{RF}}$ -driven signal phases through the quasiuniform magnetization state and across the spin-texture transition at 14 kA/m in the field-decreasing hysteresis branch. Similar to the macrospin simulation for mixed drive field components in Fig. 2(b), it was expected that bias field-dependent changes in the relative magnitudes of the EdH and cross-product torques would yield a larger bias field dependence of the phase of the net torque than we observe. The predicted phase variation at 114 MHz is smaller than that shown for 208 MHz in Fig. 2(b), but still significantly larger than observed.

Below 6.5 kA/m in the decreasing field branch, spikes in torque related to the Barkhausen effect arise. The high exchange energy density of the vortex core as well as its small diameter (approximately 10 nm) allows for high probability of interaction with pinning potentials created by magnetic disorder in the polycrystalline film. If the pinning potentials are weak enough to be overcome by thermal fluctuations, the core can experience hopping between neighboring sites [33]. The hopping rates at room temperature are generally high in comparison to the mechanical detection bandwidths. The superposition of the random disorder potential for the core with continuous tilting from the external bias field can yield circumstances during the hysteresis sweep where the energy barrier is such that thermal activation assists the core in hopping synchronously with the in-plane drive. If the associated

change in the  $y$  moment is larger than normal, this results in a spike in torque with a change in phase arising also through the thermal assist [27]. These features recur across multiple hysteresis measurements when the same bias field conditions are reproduced. Hysteresis in the low-field regime is isolated in the Supplemental Material to illustrate these features [30].

Whereas  $H_y^{\text{RF}}$  modulates the core position laterally along the sample surface, the  $H_z^{\text{RF}}$  drive minimally perturbs the core aside from small fluctuations of its width. This is reflected in the absence of Barkhausen signatures in Figs. 4(a) and 4(b). Some peaks seen in the 114 MHz signal are from the small admixture of cross product and EdH torques due to a nonzero component of in-plane ( $H_y^{\text{RF}}$ ) magnetic field in the  $I_z^{\text{RF}}$  drive (Supplemental Material [30]). With increasing detection frequencies, the Barkhausen effect features become more pronounced and larger in magnitude with respect to the overall hysteresis curve, with corresponding increase in phase modulation.

## B. Measurements at 208 MHz mode: EdH torque at a gyrotropic resonance

The  $I_y^{\text{RF}}$ -driven magnetic hysteresis measured at the 208 MHz mechanical mode [Fig. 1(e)] in Fig. 5 is at the highest frequency implemented for cantilever-style mechanical torque magnetometry to date. Empirically, our torque detection sensitivity decreases approximately as  $e^{-0.025f}$  with increasing frequency ( $f$  in MHz). The optimized signals for  $I_z^{\text{RF}}$  drives of 180 mV RMS from the lock-in amplifier through an ENI 510L power amplifier at  $H_x = 53$  kA/m were  $1104 \pm 8$   $\mu\text{V}$ ,  $656 \pm 3$   $\mu\text{V}$ ,  $248 \pm 1$   $\mu\text{V}$ , and  $62.1 \pm 0.9$   $\mu\text{V}$  for the 3, 21, 64, and 114 MHz modes. Further reduced mechanical transduction of the 208 MHz mode yielded difficulty in finding the signal through the usual procedure of optimizing the drive frequency, laser wavelength tuning, and fiber dimple positioning at high bias field with  $I_z^{\text{RF}}$  drive. Nature did us a favor, however, and arranged for the presence of a huge torque signal at low bias field through an overlap of the 208 MHz mechanical mode with an in-plane RF field driven spin resonance in the permalloy island.

The sweep from high to low field [Fig. 5(a)] follows a similar trend as seen for the in-plane  $H_y^{\text{RF}}$ -driven modes in Fig. 4(c) until the spin texture nucleates a magnetic vortex. In the vortex spin texture, the torque signal is substantially larger than that observed for the other measured in-plane  $I_y^{\text{RF}}$ -driven modes, peaking at around 4 kA/m. This is due to mechanical transduction of a spin resonance mode of the vortex texture, where the in-plane field drives the vortex core into a gyrotropic orbit [34,35]. Abrupt reduction of the RF torque occurs at certain fields where the vortex core becomes strongly pinned by magnetic disorder in the sample. For a vortex core in a thin film, out-of-plane fields do not contribute to translation of the vortex core and hence will not contribute to gyromagnetic precession. Therefore, no amplification of the 208 MHz  $I_z^{\text{RF}}$ -driven torques is expected as the result of spin resonance. Paired with the poor mechanical transduction of the high-order resonant modes and high RF background, the cross product torque component of the  $I_z^{\text{RF}}$ -driven torque is minimal (see Supplemental Material [30]).

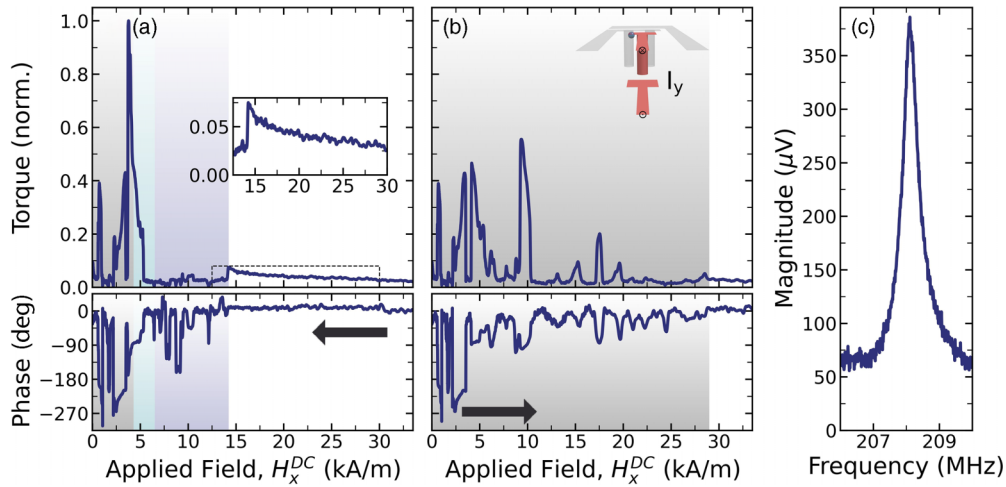


FIG. 5. Hysteresis of the 208 MHz mechanical mode through magnetic resonance.  $I_y^{\text{RF}}$ -driven hysteresis of the highest-frequency measured mode from (a) high to low and (b) low to high field. The accompanying phase is shown below the magnitude. Distinct spin textures are indicated as in Fig. 4. The high-field regime ( $H_x^{\text{dc}} > 12.5$  kA/m) is isolated in the inset of (a) to highlight the familiar hysteresis shape as seen in the lower-frequency  $I_y^{\text{RF}}$ -driven hysteresis of Fig. 4(c). The mechanical resonance measured at the peak of the hysteresis loop (around 4 kA/m).

The existence of the gyrotropic mode was confirmed through a series of micromagnetic simulations of the sample geometry (performed with MUMAX3, an open-source, GPU-based LLG solver [36]). The spin texture at 1.67 kA/m was first acquired by running a hysteresis simulation from high to low field to promote spin textures seen in experiment. In a separate simulation, a 1 ns wide, 0.398 A/m Heaviside square pulse in the plane of the sample was applied to the spin texture and the magnetization was allowed to relax. The FFT magnitude [Fig. 6(a)] of the resulting time trace of the net  $y$  torque [conventional plus EdH torques, Fig. 6(b)] demon-

strates a broad magnetic resonance which overlaps the narrow bandwidth of measured torque [shaded band in Fig. 6(a)]. The coincidence of magnetic and mechanical resonances persists over a wide applied field range, as indicated by repeating the aforementioned simulations at 2.86 kA/m and 4.06 kA/m [Fig. 6(a)]. This field range encompasses the experimental field range wherein a single vortex state is roughly centered in the permalloy mushroom.

Gyrotropic frequencies in polycrystalline permalloy microstructures are strongly modified by the imprint of magnetic disorder on the energy of the vortex core versus position, aided by field tuning of the resonance (a gradual change of the gyrotropic frequency with field in the vortex state, and enhanced by interaction of the vortex core with pinning sites in the permalloy). Local pinning potentials are caused by variations in film thickness due to granularity and in the strength of exchange coupling between grains. The frequencies of small amplitude gyrotropic orbits increase on account of the local curvature of core energy versus position, which can be significantly larger than the global curvature, owing to the overall shape of the magnetic structure and of the spin configuration within it. Mapping the gyrotropic frequency versus applied field then yields a map of the static, random potential. If the pinning is not too strong, then at some bias fields, and for strong enough RF drive, the core will manage to surf over the disorder at a gyrotropic frequency close to that expected for a perfectly uniform film.

We further elucidate the specific effects of pinning and depinning of the gyrotropic mode on magnetic torque through simulations from low to high field with a 20-nm-diameter cylindrical defect positioned along the trajectory of the vortex core within the permalloy island (see Supplemental Material for simulation details [30]). The defect mimics magnetic disorder using a slightly reduced  $M_s$  for the defect, providing a lower energy position for the vortex core to become trapped at over a small bias field range. As the core approaches the pinning site, the gyrotropic orbit elongates and the frequency decreases, as seen in Fig. 7. The energy minimum of the

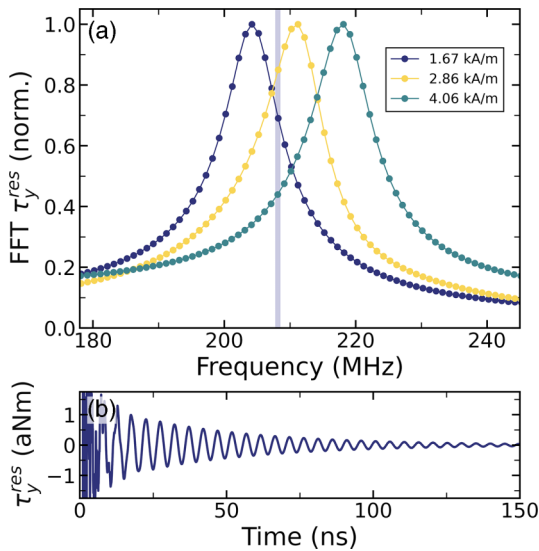


FIG. 6. Micromagnetic simulations of torque across the gyrotropic resonance for several dc bias fields. FFT calculations of micromagnetic simulation output for a 1 ns field pulse applied to the single-vortex state at three distinct bias fields are shown in (a). The shaded vertical bar indicates the frequency and linewidth of the measured mechanical resonance from Fig. 5(b). The time trace of resultant torque at 1.67 kA/m bias field is shown in (b).

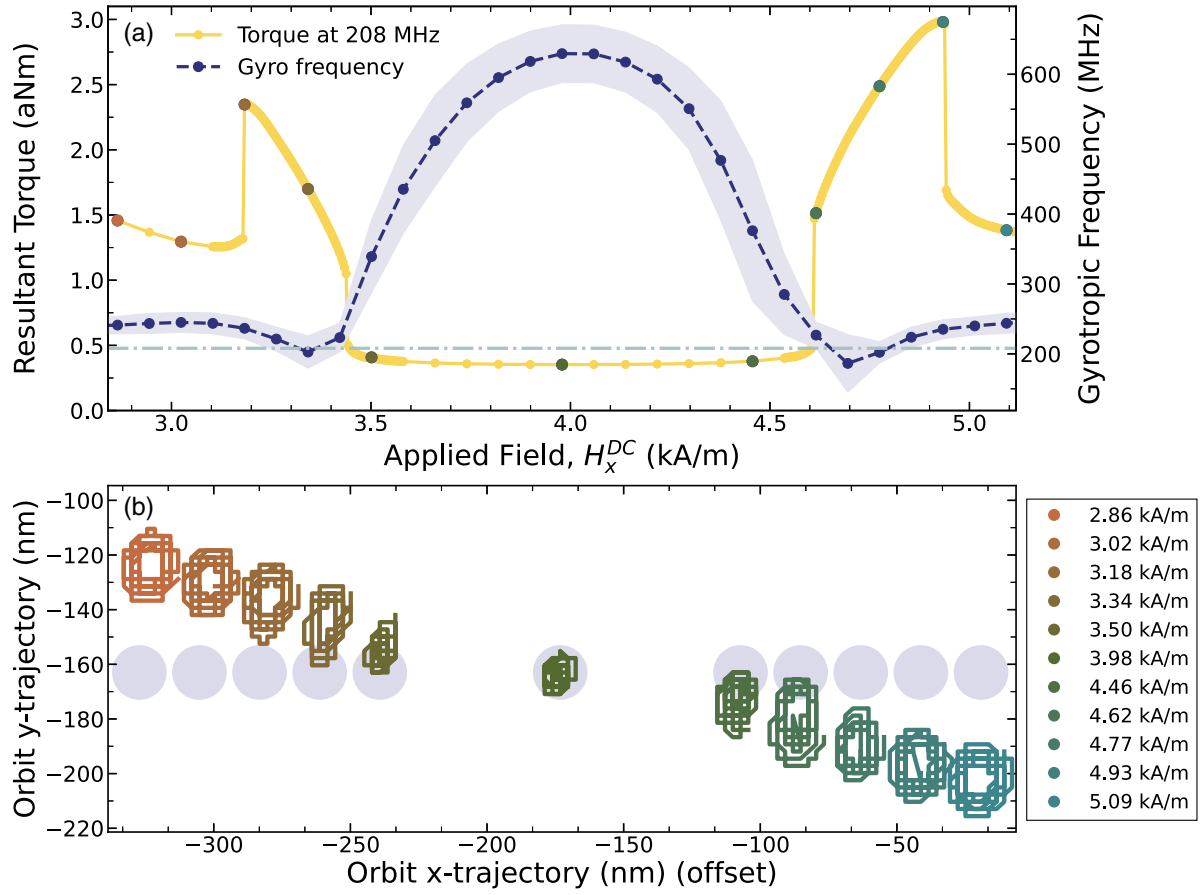


FIG. 7. Simulated  $H_y^{\text{RF}}$ -driven torques at 208 MHz in the vicinity of a vortex core pinning site. (a) Simulated torque (yellow curve) from low to high field for a time-evolving micromagnetic simulation with a defect positioned in the path of the vortex core. The local gyrotropic frequency, shown in purple and plotted against the right-hand vertical axis, is strongly and nonmonotonically position (bias field) dependent outside of and within the pinning site. The 208 MHz driving frequency is indicated by the horizontal blue line. As an aid in visualizing the origin of the resultant, predominantly EdH torque, the core trajectories for 11 of the specific driven gyrotropic motions are shown in (b), corresponding to the discrete field points indicated on the torque curve in (a). The defect location is offset along the  $x$  axis for each dc field value, indicated by light blue circles.

pinning site behaves like an attractor and adds additional angular momentum to the core as it nears the defect, in an approximate parallel to a gravitational slingshot. Direct interaction with the pinning site reduces angular momentum (and therefore the torque) due to the energy cost required to exit the defect's influence. The reduced energy requirements inside the defect leads to a significant increase in gyrotropic frequency, with maximum frequency occurring when the orbit is centered within the defect. The effect of an additional pinning site along the core's trajectory is explored in the Supplemental Material, wherein general agreement of phase and magnitude behavior between measured and simulated torques is observed [30].

### III. GLOBAL MODEL OF TORQUE MAGNITUDES AND PHASES IN THE QUASIUNIFORM SPIN TEXTURE

The admixture of the  $z$  field from the  $H_y^{\text{RF}}$  coil has a prominent effect on measured torques. COMSOL simulation of the field produced by the coil geometry (Fig. 3) indicates an opposite sign of  $H_z^{\text{RF}}$  relative to  $H_y^{\text{RF}}$  at the sample position when driving the  $H_y^{\text{RF}}$  coil. Because of the importance of

signal phases, this must be incorporated into micromagnetic simulations by including the sign of the field ratio and computing the superposition of  $-H_z$ -driven torques, scaled by the field ratio, with  $H_y$ -driven torques. The effect of this is evident in Fig. 8, in which the high-field portion of the measured hysteresis is isolated and compared to these simulations. The simulated, admixed signal phase slopes downwards to higher bias fields, in qualitative agreement with the phase slopes observed in the measured torques (opposite to what was seen for a positive ratio admixture in Fig. 2).

A global comparison at all frequencies of the raw, simulated admixture torques shows poor quantitative correspondence to measured torques over the 14 to 53 kA/m field range, corresponding to the quasi-uniform spin texture field-decreasing branch (Fig. 8). At the upper field limit of this spin texture, the  $H_z$ -driven torques dominate and admixture of  $H_y$  contributes little to the torque. Closer to nucleation of a vortex core at the lower field limit of the quasiuniform spin texture, the  $H_y$ -driven torques play a larger role. In this region, the correspondence between simulation and experiment weakens. The quantitative distinctions, which show up with greater contrast at higher frequencies where the EdH torque

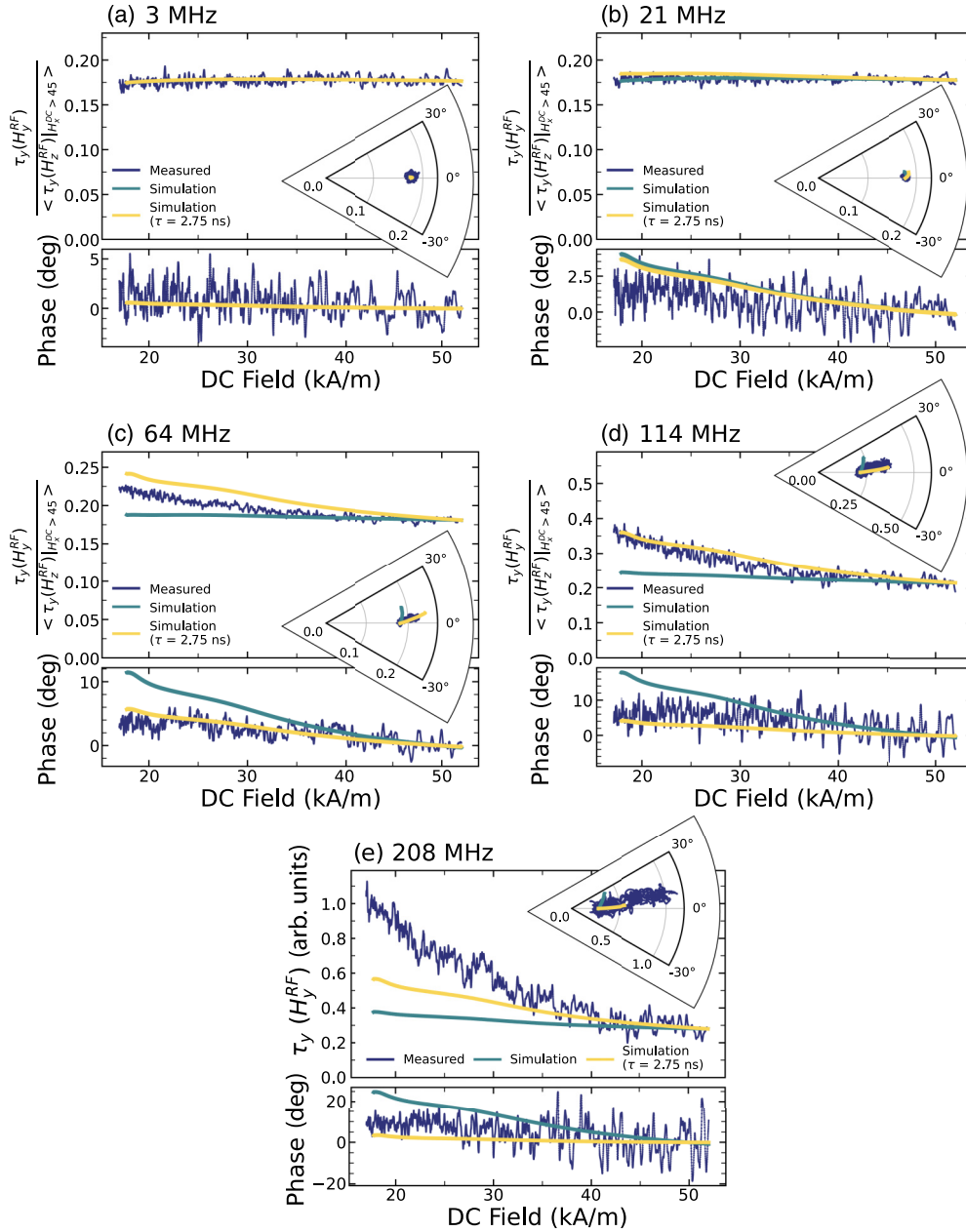


FIG. 8. High-field hysteresis and micromagnetic simulation. Experimental torque signals (purple) as presented in Fig. 3 in the main text compared against simulation output for primarily  $H_y^{RF}$ -driven torques superimposed with a small  $-H_z^{RF}$  drive contribution ( $-25.2\%$  of the  $H_y^{RF}$  contribution). The opposite sign of  $H_z^{RF}$  and  $H_y^{RF}$  is indicated by simulation of the field vector at the sample location Fig. 3, contrary to macrospin simulation output presented in Fig. 2(b), where the admixed field components have the same relative phase. An exponentially weighted mean with time constant  $\tau = 2.75$  ns is applied to the  $H_z^{RF}$ -driven simulation torque (yellow) to mimic the effect of a relaxation process in the cross product torque. This relaxation process empirically improves agreement to measured torques in comparison to the nonfiltered combination (green). Insets of polar segments provide an alternate view of the experiment/model comparison, illustrating the heightened agreement through filtering.

contribution is larger, are that the experimental phase has less overall field slope than simulations, and that the simulated, resultant torque magnitudes have less overall field slope than found from experiments. Taken together, these quantitative differences point in the direction of a breakdown of the strict phase orthogonality ( $\pi/2$  relative phase difference) between the EdH and cross-product torques within the frequency range of this study. In the phasor superposition of a smaller but growing torque component with a larger and constant com-

ponent, the overall magnitude (phase) variation will increase (decrease) when the relative phase difference between the two moves away from  $\pi/2$ . A likely cause for this behavior is the decoupling of internal phonon modes from the rigid body rotation of the resonator [7].

Timescales for magnetic torques are a topic of considerable current interest. With ultrafast x-ray observations of phonon generation by EdH torque on subpicosecond timescales [37], we assume that the EdH mechanical torques are effectively

instantaneous at our frequencies of measurement (although the question of bottlenecks due to the cascade from short- to long-wavelength phonons remains open). The timescale for mechanical torque generation from shape anisotropy alone (the composition of  $\text{Ni}_{80}\text{Fe}_{20}$  is tailored to minimize magnetoelastic response) are undetermined, to our knowledge. Phenomenologically, a single pole low-pass filter is the simplest model addition to add phase shifting between a cross product magnetic shape anisotropy torque and its resulting rigid body mechanical torque. In an circuit analogy, we envision the RF magnetic torque as an ac current source driving a parallel RC circuit, where the RC integrator time constant mimics the time dependence of torque conversion and the current in the resistor represents the rigid body mechanical torque.

The RC circuit model is included using a circuit time constant of 2.75 ns (within the range of 0.5–4 ns constrained by experiment). This model is applied to simulations via an exponentially weighted mean function acting on the  $H_z$ -driven torque to act as the RC filter. The filtered  $H_z$ -driven torques are superimposed with a  $H_y$ -driven torque with relative drive field strengths in agreement with COMSOL simulations of the driving coils. This procedure pushes simulations to closer agreement with experiment (Fig. 8) by increasing (decreasing) the overall slope of the magnitude (phase). This agreement is observed plainly in the polar insets of Fig. 8, which show the filtered simulations mapping directly to measurement, contrary to behavior observed in unfiltered simulations. The 208 MHz simulations have notably worse agreement in torque magnitude than the lower order modes. This can be attributed in part to softening of the spin texture before nucleation of the vortex, as closure domains near the edges of the mushroom shape become trapped. This trapping produces different resonance behavior than expected for a uniformly magnetized sample. Simulation of FMR of the mushroom shape in the 18 to 25 kA/m field range supports this explanation, revealing broad frequency signatures near 200 MHz for an excitation in the  $H_y$  drive which will interact with the 208 MHz drive frequency.

#### IV. CONCLUSION

To summarize, nanocavity optomechanical sensing extends the mechanical detection (and corresponding ac magnetic

drive) frequency range beyond previous studies by almost two orders of magnitude in the measurements reported here. This opens two additional regimes to EdH observations: torques generated by ac perturbation of the direction of the moment in magnetically saturated specimens and nonequilibrium torques boosted by a collective mode of the magnetization at the mechanical detection frequency.

Current experimental limitations prohibit sample translation relative to the excitation coils. Ongoing studies will incorporate such adjustments to provide an independent measure of the relative phase between the  $H_y$ - and  $H_z$ -driven torque responses, e.g., by recording the torque magnitude and phase after translating the sample across the y coil to change the sign of the  $H_z^{\text{RF}}$  admixture (equivalent to changing its phase by  $180^\circ$ ). Determination of the absolute phases of the drive fields at the sample location will also be valuable and can be accomplished using a magneto-optical probe. Employing a phase-locked loop during measurement will prevent any thermally induced frequency shifts from insidiously affecting measured torques. Including an additional axis of driving field would allow further excitation of the gyrotropic mode to expand this study with the caveat that, with the current field geometry, no further low-frequency torques could be excited in this manner. Adjusting the field geometry or utilizing a sensor boasting mechanical compliance to an additional torque axis are reasonable solutions to be employed in related studies. Additionally, future work will be performed at low temperatures to eliminate the slower, thermally activated dynamics and thereby simplifying the observations.

The code that supports this paper including the macrospin simulation, lock-in emulator, MUMAX3 scripts, and processing scripts are available via GitHub at Ref. [38].

#### ACKNOWLEDGMENTS

The authors gratefully acknowledge support from the Natural Sciences and Engineering Research Council, Canada (No. RGPIN-2021-02762), the Canada Foundation for Innovation (No. 34028), the Canada Research Chairs (No. 230377), the National Research Council (Canada), and the University of Alberta.

K.R.F. and J.E.L. contributed equally to this work.

- 
- [1] A. Einstein and W. J. de Haas, in *KNAW, Proceedings* (Dutch History of Science Web Centre, 1915), Vol. 18 I, pp. 696–711.
  - [2] T. M. Wallis, J. Moreland, and P. Kabos, *Appl. Phys. Lett.* **89**, 122502 (2006).
  - [3] R. Jaafar, E. M. Chudnovsky, and D. A. Garanin, *Phys. Rev. B* **79**, 104410 (2009).
  - [4] E. M. Chudnovsky and D. A. Garanin, *Phys. Rev. B* **89**, 174420 (2014).
  - [5] R. Zarzuela and E. M. Chudnovsky, *J. Supercond. Novel Magn.* **28**, 3411 (2015).
  - [6] T. Wells, A. P. Horsfield, W. M. Foulkes, and S. L. Dudarev, *J. Chem. Phys.* **150**, 224109 (2019).
  - [7] A. Rückriegel, S. Streib, G. E. W. Bauer, and R. A. Duine, *Phys. Rev. B* **101**, 104402 (2020).
  - [8] K. Mori, M. G. Dunsmore, J. E. Losby, D. M. Jenson, M. Belov, and M. R. Freeman, *Phys. Rev. B* **102**, 054415 (2020).
  - [9] D. A. Garanin and E. M. Chudnovsky, *Phys. Rev. B* **103**, L100412 (2021).
  - [10] W. Dednam, C. Sabater, A. E. Botha, E. B. Lombardi, J. Fernández-Rossier, and M. J. Caturla, *Comput. Mater. Sci.* **209**, 111359 (2022).
  - [11] J. S. Brooks, M. J. Naughton, Y. P. Ma, P. M. Chaikin, and R. V. Chamberlin, *Rev. Sci. Instrum.* **58**, 117 (1987).
  - [12] A. N. Cleland and M. L. Roukes, *Appl. Phys. Lett.* **69**, 2653 (1996).
  - [13] D. W. Carr and H. Craighead, *J. Vac. Sci. Technol. B* **15**, 2760 (1997).

- [14] G. Alzetta, C. Ascoli, P. Baschieri, D. Bertolini, I. Betti, B. D. Masi, C. Frediani, L. Lenci, M. Martinelli, and G. Scalari, *J. Magn. Reson.* **141**, 148 (1999).
- [15] J. Moreland, A. Jander, J. A. Beall, P. Kabos, and S. E. Russek, *IEEE Trans. Magn.* **37**, 2770 (2001).
- [16] A. Jander, J. Moreland, and P. Kabos, *Appl. Phys. Lett.* **78**, 2348 (2001).
- [17] J. E. Losby, V. T. K. Sauer, and M. R. Freeman, *J. Phys. D: Appl. Phys.* **51**, 483001 (2018).
- [18] K. Harii, Y.-J. Seo, Y. Tsutsumi, H. Chudo, K. Oyanagi, M. Matsuo, Y. Shiomi, T. Ono, S. Maekawa, and E. Saitoh, *Nat. Commun.* **10**, 2616 (2019).
- [19] M. Eichenfield, R. Camacho, J. Chan, K. J. Vahala, and O. Painter, *Nature (London)* **459**, 550 (2009).
- [20] P. H. Kim, C. Doolin, B. D. Hauer, A. J. MacDonald, M. R. Freeman, P. E. Barclay, and J. P. Davis, *Appl. Phys. Lett.* **102**, 053102 (2013).
- [21] M. Aspelmeyer, T. J. Kippenberg, and F. Marquardt, *Rev. Mod. Phys.* **86**, 1391 (2014).
- [22] S. Forstner, E. Sheridan, J. Knittel, C. L. Humphreys, G. A. Brawley, H. Rubinsztein-Dunlop, and W. P. Bowen, *Adv. Mater.* **26**, 6348 (2014).
- [23] B.-B. Li, G. Brawley, H. Greenall, S. Forstner, E. Sheridan, H. Rubinsztein-Dunlop, and W. P. Bowen, *Photonics Res.* **8**, 1064 (2020).
- [24] A. A. Kovalev, G. E. W. Bauer, and A. Brataas, *Phys. Rev. Lett.* **94**, 167201 (2005).
- [25] A. A. Kovalev, G. E. W. Bauer, and A. Brataas, *Jpn. J. Appl. Phys.* **45**, 3878 (2006).
- [26] M. Wu, N. L. Y. Wu, T. Firdous, F. Fani Sani, J. E. Losby, M. R. Freeman, and P. E. Barclay, *Nat. Nanotechnol.* **12**, 127 (2017).
- [27] G. Hajisalem, J. E. Losby, G. de Oliveira Luiz, V. T. K. Sauer, P. E. Barclay, and M. R. Freeman, *New J. Phys.* **21**, 095005 (2019).
- [28] A. C. Hryciw and P. E. Barclay, *Opt. Lett.* **38**, 1612 (2013).
- [29] COMSOL Multiphysics® v 6.1., [www.comsol.com](http://www.comsol.com). COMSOL AB, Stockholm, Sweden.
- [30] See Supplemental Material at <http://link.aps.org/supplemental/10.1103/PhysRevB.109.064404> for further information on data processing techniques, macrospin simulation details, and Mumax<sup>3</sup> simulation details.
- [31] S.-H. Lim, A. Imtiaz, T. M. Wallis, S. Russek, P. Kabos, L. Cai, and E. M. Chudnovsky, *Europhys. Lett.* **105**, 37009 (2014).
- [32] R. P. Cowburn, D. K. Koltsov, A. O. Adeyeye, M. E. Welland, and D. M. Tricker, *Phys. Rev. Lett.* **83**, 1042 (1999).
- [33] J. A. J. Burgess, A. E. Fraser, F. Fani Sani, D. Vick, B. D. Hauer, J. P. Davis, and M. R. Freeman, *Science* **339**, 1051 (2013).
- [34] R. L. Compton and P. A. Crowell, *Phys. Rev. Lett.* **97**, 137202 (2006).
- [35] R. L. Compton, T. Y. Chen, and P. A. Crowell, *Phys. Rev. B* **81**, 144412 (2010).
- [36] A. Vansteenkiste, J. Leliaert, M. Dvornik, M. Helsen, F. Garcia-Sanchez, and B. Van de Wiele, *AIP Adv.* **4**, 107133 (2014).
- [37] C. Dornes, Y. Acremann, M. Savoini, M. Kubli, M. J. Neugebauer, E. Abreu, L. Huber, G. Lantz, C. A. F. Vaz, H. Lemke, E. M. Bothschafter, M. Porer, V. Esposito, L. Rettig, M. Buzzi, A. Alberca, Y. W. Windsor, P. Beaud, U. Staub, D. Zhu *et al.*, *Nature (London)* **565**, 209 (2019).
- [38] [https://github.com/KatrynaFast/EdH\\_DiscreteSpectroscopicProbe\\_Analysis-info](https://github.com/KatrynaFast/EdH_DiscreteSpectroscopicProbe_Analysis-info).